


# Research on the static fission properties of $^{240}\text{Pu}$ within the reflection asymmetric relativistic mean-field theory

Yu-Ting Qiu and Jian-You Guo <sup>\*</sup>

*School of Physics and Optoelectronics Engineering, Anhui University, Hefei 230601, People's Republic of China*

 (Received 4 November 2023; revised 31 January 2024; accepted 15 March 2024; published 1 April 2024)

The reflection asymmetric relativistic mean-field (RASRMF) theory was applied to investigate the static fission properties of  $^{240}\text{Pu}$ . The potential energy curves with different spatial symmetries were obtained, and the calculated fission barrier heights are in good agreement with available experimental data. Compared with other theoretical calculations, better consistency with experiments is achieved. The matter density distributions clearly show the shape evolution along the fission path. Notably, the outer barrier is significantly reduced due to the reflection asymmetric deformations, making mass-asymmetric fission more favorable. These results indicate that the reflection asymmetric degree of freedom plays an important role in regulating the fission barrier and fission path of  $^{240}\text{Pu}$ . Furthermore, the sensitivity of fission barriers to pairing correlations was examined. The use of the BCS approximation with a constant pairing gap led to unphysical results; therefore, a variable pairing strength was used to evaluate its influence on the fission barriers. It was found that a slight increase in pairing strength enhanced ground state stability but reduced fission barrier heights, promoting fission through more effective state repopulation during nuclear elongation. This conclusion remains consistent across RASRMF calculations employing both the NL3 and PK1 parameters.

DOI: [10.1103/PhysRevC.109.044301](https://doi.org/10.1103/PhysRevC.109.044301)

## I. INTRODUCTION

The atomic nucleus is a complex quantum many-body system with intricate interparticle interactions. Nuclear fission [1,2], which is related to quantum tunneling resulting from a nonequilibrium large amplitude collective motion in the system, is one of the most enigmatic phenomena in modern nuclear physics. The first experimental evidence of nuclear fission was discovered by Hahn and Strassman in 1939 [3]. Meitner and Frisch [4], as well as Bohr and Wheeler [5], provided theoretical interpretations of the process shortly thereafter. Since then, numerous studies have focused on the fission mechanism. These explanations suggest that the competition between nuclear attraction and Coulomb repulsion drives the nucleus to split into two or three fragments that subsequently decay by emitting particles. Despite extensive investigations into the fission mechanism, a fully microscopic description of the process remains extremely challenging.

To comprehend nuclear fission, it is essential to have a comprehensive understanding of the fission barrier, such as its height, which plays a crucial role in comprehending the mechanisms and dynamics of nuclear fission and estimating the corresponding observables quantitatively [6–10]. The fission barrier is also related to the stability of superheavy nuclei [11–14] and the  $r$  process of stellar nucleosynthesis [15–17]. Actinide nuclei are primarily characterized by a double-humped fission barrier due to quantum shell effects [18–20]. The inner and outer barriers can be affected

differently through various deformation degrees of freedom. Triaxial and octupole deformations can decrease the heights of the inner and outer barriers, respectively [21–23]. Since the fission barrier is not observable, and the height of the fission barrier is model dependent, it is necessary to compare various theoretical models to obtain a more reliable fission barrier.

The liquid-drop model [5], proposed by Bohr and Wheeler, was the first model for describing the fission barriers. They used this model to calculate barrier heights and associated deformations for extremely heavy nuclei. To explain the experimental observation that fission mainly occurs asymmetrically, microscopic shell corrections were introduced to the liquid-drop model by Strutinsky and his collaborators [18,19]. The macroscopic-microscopic (MM) method, which derives from the Strutinsky shell correction method, is an important candidate for large-scale calculations of fission barriers based on the analysis of multidimensional potential energy surfaces. To date, several versions of the MM method have been developed to study fission barriers, including the MM finite-range liquid-drop model [24–26], the MM Woods-Saxon model [27–30], the MM Lublin-Strasbourg drop model [31–33], and the MM cranked Nilsson-Strutinsky model [34]. In addition, there are also some microscopic methods, such as the extended Thomas-Fermi plus Strutinsky integral method [16,35,36], nonrelativistic energy density functionals based on Skyrme [37–40] and Gogny forces [41–44], and covariant density functional theory [45–51], for examining fission barriers.

As previously mentioned, the majority of research on fission barriers has been conducted using nonrelativistic models. In recent years, covariant density functional theory (CDFT)

<sup>\*</sup>Corresponding author: [jianyout@ahu.edu.cn](mailto:jianyout@ahu.edu.cn)

[52–55] has emerged as one of the most successful microscopic models for studying both ground and excited states of nuclei across the entire nuclear chart. Specifically, CDFT in the deformed harmonic oscillator (HO) basis has been widely applied to investigate fission barriers and has yielded results consistent with experimental data [56–61]. For example, Abusara *et al.* [57] conducted the first systematic investigation of inner fission barriers for actinide nuclei within the triaxial relativistic mean-field approach in a Cartesian deformed HO basis. Subsequently, similar studies were extended to superheavy nuclei by Abusara *et al.* [62]. To examine the impact of triaxial and octupole deformations on even-even actinide fission barriers, Lu *et al.* [59] developed a multidimensional constrained CDFT in an axially deformed HO basis. However, due to the complexity of large deformation configurations during fission, the accuracy of calculations based on the one-center HO basis decreases with increasing elongation. The two-center HO (TCHO) basis is one option to address this problem and has been used in nonrelativistic Hartree-Fock-Bogoliubov models [63–65] and the MM model [33]. TCHO has proven to be particularly suitable for describing fission systems. Recently, TCHO has also been extended in point-coupling CDFT to analyze induced fission dynamics [66].

The impact of triaxiality on the fission barrier has long been recognized. In macroscopic-microscopic model calculations, the introduction of triaxial deformation can reduce the height of the inner fission barrier [21,22,30,67]. Similarly, in nonrelativistic and relativistic energy density functional calculations, triaxial deformation significantly affects the height of the fission barrier for actinides [41,57,58,68–70]. Typically, the lowering effect of triaxiality on the inner barrier of actinides is around 1–3 MeV [49], while that on the outer barrier is approximately 0.5–1 MeV [59,71]. For superheavy nuclei, the influence of triaxial deformation on fission is even more pronounced [14]. Therefore, it is evident that triaxiality plays a crucial role in nuclear fission.

In addition to triaxiality, reflection asymmetric octupole deformation also has a significant impact on fission. It is well known that the heights of the outer barriers of actinide nuclei can be reduced by octupole deformation. Furthermore, studies have shown that including octupole deformation can lead to a transition from mass-symmetric to mass-asymmetric fission for actinides and superheavy nuclei [72,73]. Octupole-deformed shell effects are primarily responsible for mass-asymmetric fission in actinides [74]. Here, we mainly focus on the influence of octupole deformation on fission, and ignore the triaxial deformation in order to clearly demonstrate the importance of octupole deformation to fission.

The reflection asymmetric relativistic mean-field (RASRMF) theory based on the TCHO basis has been employed to study octupole deformed nuclei [75] and has successfully described octupole shape phase transition [76,77] and shape coexistence phenomena [78,79]. This work aims to better understand the role of octupole deformation in the fission process by examining the static fission properties of  $^{240}\text{Pu}$  using the RASRMF theory and to provide a more accurate description for experimental data on fission barriers in actinides. Furthermore, considering the important role that pairing

correlations play in the fission process of atomic nuclei, it is essential to appropriately address pairing correlations in order to obtain reliable fission barriers. We have compared various strategies for addressing pairing correlations within the BCS approximation and have proposed a more suitable approach for their consideration.

The paper is organized as follows: Sec. II provides an overview of the RASRMF theory, Sec. III presents the numerical details and results, and Sec. IV offers a summary of the findings.

## II. FORMALISM

To investigate the fission properties for  $^{240}\text{Pu}$ , we first present the theoretical formalism of RASRMF. The starting point of the RASRMF theory is an effective Lagrangian density [80–82]:

$$\begin{aligned} \mathcal{L} = & \bar{\psi}[i\gamma^\mu \partial_\mu - M - g_\sigma \sigma - g_\omega \omega_\mu \gamma^\mu - g_\rho \vec{\rho}_\mu \vec{\tau} \gamma^\mu \\ & - \frac{1}{2}e\gamma^\mu (1 - \tau_3)A_\mu]\psi + \frac{1}{2}(\partial_\mu \sigma \partial^\mu \sigma - m_\sigma^2 \sigma^2) \\ & - \frac{1}{4}\omega^{\mu\nu} \omega_{\mu\nu} + \frac{1}{2}m_\omega^2 \omega^\mu \omega_\mu - \frac{1}{3}g_2 \sigma^3 - \frac{1}{4}g_3 \sigma^4 \\ & - \frac{1}{4}\vec{\rho}^{\mu\nu} \vec{\rho}_{\mu\nu} + \frac{1}{2}m_\rho^2 \vec{\rho}^\mu \vec{\rho}_\mu + \frac{1}{4}c_3 (\omega^\mu \omega_\mu)^2 \\ & - \frac{1}{4}A^{\mu\nu} A_{\mu\nu}, \end{aligned} \quad (1)$$

where  $\psi$  is the Dirac spinor of the nucleon with the corresponding mass  $M$ ,  $\sigma$  is the isoscalar-scalar meson that provides medium-range attraction,  $\omega$  is the isoscalar-vector meson that provides short-range repulsion,  $\rho$  is the isovector-vector meson reflecting the difference of neutron and proton, and  $A$  is the photon field describing the electromagnetic properties of atomic nuclei.  $m_\sigma$ ,  $m_\omega$ , and  $m_\rho$  are the masses of  $\sigma$ ,  $\omega$ , and  $\rho$  mesons, and  $g_\sigma$ ,  $g_\omega$ , and  $g_\rho$  are the coupling constants of the mesons with the nucleons.  $g_2$ ,  $g_3$ , and  $c_3$  are the nonlinear self-coupling coefficients of  $\sigma$  and  $\omega$  mesons. The field tensors for the mesons and photons are defined as

$$\begin{aligned} \omega^{\mu\nu} &= \partial^\mu \omega^\nu - \partial^\nu \omega^\mu, \\ \vec{\rho}^{\mu\nu} &= \partial^\mu \vec{\rho}^\nu - \partial^\nu \vec{\rho}^\mu, \\ A^{\mu\nu} &= \partial^\mu A^\nu - \partial^\nu A^\mu. \end{aligned}$$

Starting from the Lagrangian density, with the classical variational principle, we derive the Dirac equation

$$[-i\vec{\alpha} \cdot \vec{\nabla} + V(\vec{r}) + \beta[M + S(\vec{r})]]\psi_i = \epsilon_i \psi_i \quad (2)$$

for the nucleons with the scalar potential  $S(\vec{r})$  and vector potential  $V(\vec{r})$ ,

$$S(\vec{r}) = g_\sigma \sigma(\vec{r}),$$

$$V(\vec{r}) = g_\omega \omega_0(\vec{r}) + g_\rho \tau_3 \rho_0(\vec{r}) + e \frac{(1 - \tau_3)}{2} A_0(\vec{r}),$$

and the Klein-Gordon equations

$$(-\Delta + m_\sigma^2)\sigma = -g_\sigma \rho_s - g_2 \sigma^2 - g_3 \sigma^3,$$

$$(-\Delta + m_\omega^2)\omega_0 = g_\omega \rho_v - c_3 \omega_0^3,$$

$$(-\Delta + m_\rho^2)\rho_0 = g_\rho \rho_3,$$

$$-\Delta A_0 = e \rho_c \quad (3)$$

for the mesons and photons with the source terms

$$\begin{aligned}\rho_s &= \sum_{i=1}^A \bar{\psi}_i \psi_i, \quad \rho_v = \sum_{i=1}^A \psi_i^\dagger \psi_i, \\ \rho_3 &= \sum_{i=1}^A \psi_i^\dagger \tau_3 \psi_i, \quad \rho_c = \sum_{p=1}^Z \psi_p^\dagger \psi_p.\end{aligned}$$

Equations (2) and (3) are nonlinear coupled equations, and solved by the basis expansion method. For the axially symmetric deformed nuclei, the Dirac spinors can be presented as

$$\begin{aligned}\psi_i(r, t) &= \begin{pmatrix} f_i(r, s, t) \\ ig_i(r, s, t) \end{pmatrix} \\ &= \frac{1}{\sqrt{2\pi}} \begin{pmatrix} f_i^+(z, r_\perp) e^{i(\Omega_i - \frac{1}{2})\varphi} \\ f_i^-(z, r_\perp) e^{i(\Omega_i + \frac{1}{2})\varphi} \\ ig_i^+(z, r_\perp) e^{i(\Omega_i - \frac{1}{2})\varphi} \\ ig_i^-(z, r_\perp) e^{i(\Omega_i + \frac{1}{2})\varphi} \end{pmatrix} x_i(t), \quad (4)\end{aligned}$$

where  $\Omega_i$  is the third component of angular momentum. To include the reflection asymmetric degree of freedom, the eigenfunctions of the TCHO potential are used as the basis to expand the Dirac spinors  $f_i^\pm$  and  $g_i^\pm$  in the RMF calculations. The TCHO potential [75] has the following form:

$$V(r_\perp, z) = \frac{1}{2} M \omega_\perp^2 r_\perp^2 + \begin{cases} \frac{1}{2} M \omega_1^2 (z + z_1)^2, & z < 0, \\ \frac{1}{2} M \omega_2^2 (z - z_2)^2, & z \geq 0. \end{cases} \quad (5)$$

Here,  $z_1$  and  $z_2$  represent the distances from the center of the ellipsoid to the plane of their intersection, and  $\omega_1$  ( $\omega_2$ ) corresponds to the oscillation frequency of the harmonic oscillator for  $z < 0$  ( $z \geq 0$ ).

The TCHO potential can be completely determined by the three parameters  $\delta_2$ ,  $\delta_3$ , and  $\Delta z$ .  $\delta_2$  is the basis deformation. At the large elongations encountered in the description of fission, the convergence of the numerical calculation will be poor if the selected basis deformation is not appropriate, and the obtained results may be incorrect. In the present calculation, the basis deformation is chosen in the following way [83]:  $\delta_2 = 0.5\beta_2$  for  $0 \leq \beta_2 \leq 1.5$  and  $\delta_2 = 0.5\sqrt{\beta_2}$  for  $\beta_2 > 1.5$ .  $\delta_3$  is the asymmetric coefficient of the TCHO basis,  $\delta_3 = \omega_1/\omega_2$ . When  $\delta_3 = 1$ , the system is reflection symmetric.  $\Delta z (= z_1 + z_2)$  represents the center distance of the TCHO basis. Here, we mainly focus on the reflection asymmetric deformation; the adopted  $\Delta z$  is consistent with that in Ref. [75].

Along the elongated direction, more states are included in the basis, which will be conducive to the convergence of the results. Following the prescription of Ref. [71], the states meeting  $[n_z/Q_z + (2n_\rho + |m_l|)/Q_\rho] \leq N_f$  are included in the expansion of the large component of the Dirac spinor, where  $Q_z = \max(1, b_z/b_0)$  and  $Q_\rho = \max(1, b_\rho/b_0)$ , and  $b_0$ ,  $b_z$ , and  $b_\rho$  are the oscillator lengths. The expansion of the small component is truncated at  $N_g = N_f + 1$  major shell to avoid the occurrence of spurious states.

In order to obtain the potential energy curves, i.e., the total binding energy as a function of deformation, we perform the constrained RMF calculations. The binding energy under a certain deformation can be obtained by constraining

the quadrupole moment  $\langle \hat{Q}_2 \rangle$  to the given value  $\mu_2$  in the expectation value of the Hamiltonian [84], i.e.,

$$\langle H' \rangle = \langle H \rangle + \frac{1}{2} C_2 (\langle \hat{Q}_2 \rangle - \mu_2)^2 \quad (6)$$

where  $C_2$  is the spring constant, and  $\mu_2$  is the given quadrupole moment.  $\langle \hat{Q}_2 \rangle$  is the expectation value of the quadrupole moment operator, which is expressed as  $\langle \hat{Q}_2 \rangle = \langle 2r^2 P_2(\cos\theta) \rangle$ . The deformation parameter  $\beta_2$  is related to  $\langle \hat{Q}_2 \rangle$  by  $\langle \hat{Q}_2 \rangle = \frac{3}{\sqrt{5\pi}} AR^2 \beta_2$  with  $R = r_0 A^{\frac{1}{3}}$  ( $r_0 = 1.2$  fm) and  $A$  is the mass number.

We also fix the center-of-mass of the nuclei at the origin under the constraints of the monopole moment operator  $\langle \hat{Q}_1 \rangle$  to avoid spurious motions of the center of mass:

$$\langle \hat{Q}_1 \rangle = 0. \quad (7)$$

### III. NUMERICAL DETAILS AND RESULTS

Based on the previous formalism, we investigate the static fission properties of actinide nuclei with  $^{240}\text{Pu}$  as an example. To enhance the precision of our results, we employ the updated NL3\* parameter set [85] in our calculations. Pairing correlations are handled using the traditional BCS approximation. The corresponding parameters are determined by reproducing the experimental odd-even mass difference. For the ground state of the nucleus, either a BCS approximation with a constant pairing gap or a given pairing strength is suitable. However, in the study of the fission process of atomic nuclei, it is not appropriate to use a BCS approximation with a constant pairing gap. The reasons for this will be discussed in more detail later. In the RASRMF calculation here, the pairing correlations are processed with a BCS approximation of the given pairing strength. Specifically, we set the neutron pairing strength  $G_n = 0.089178$  MeV and proton pairing intensity  $G_p = 0.144259$  MeV.

The potential energy curves of  $^{240}\text{Pu}$  as a function of the quadrupole deformation  $\beta_2$  are shown in Fig. 1. The red solid line represents the fission path obtained from the RASRMF calculations, while the black solid line shows the result from the usual reflection symmetric relativistic mean field (RSRMF) calculations for better understanding of the lowering effect of the reflection asymmetric degree of freedom on the outer barrier. Both the reflection symmetric and reflection asymmetric fission paths exhibit a double-hump structure, with the former having a higher outer barrier. However, when reflection asymmetry is considered, the outer barrier height decreases significantly, making the reflection asymmetric fission path more favorable. This finding is consistent with previous studies that emphasized the role of octupole deformation on the outer barrier [46,59]. Furthermore, it can be observed from Fig. 1 that the reflection symmetric and reflection asymmetric fission paths of  $^{240}\text{Pu}$  from the ground state to the isomeric state almost overlap, indicating that octupole deformation has little effect near the inner barrier.

In Refs. [72,73], it was shown that the inclusion of the octupole deformation in the actinides and superheavy nuclei leads to a transition from symmetric to asymmetric fission. To illustrate this transformation clearly, the matter density distributions in  $^{240}\text{Pu}$  at the ground state, first saddle point,

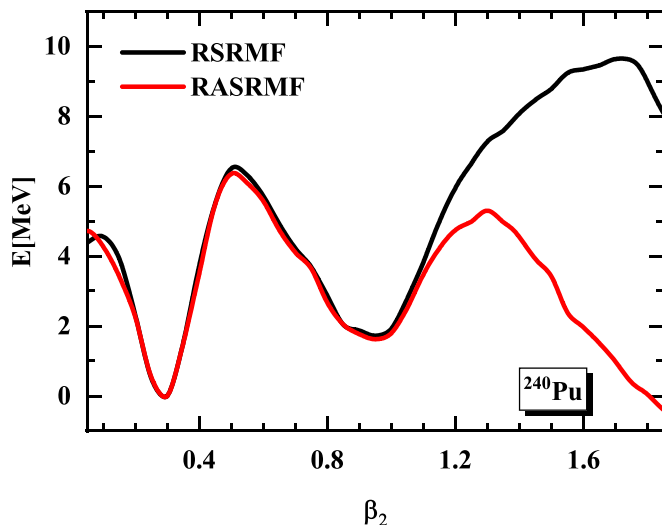


FIG. 1. Potential energy curves of  $^{240}\text{Pu}$  as a function of the quadrupole deformation  $\beta_2$ . The black solid line corresponds to the result obtained in the RSRMF calculations, and the red solid line corresponds to that obtained in the RASRMF calculations. The energy is normalized with respect to the binding energy of the ground state. The parameter set used is NL3\*.

isomeric state, and second saddle point are plotted in Fig. 2. Figures 2(a) and 2(b) correspond to the results with reflection symmetry and reflection asymmetry imposed, respectively. In Fig. 2(a), the ground state of  $^{240}\text{Pu}$  has a prolate shape. At the first saddle point of the fission path, the nucleus elongates along the  $z$  axis. As the quadrupole deformation  $\beta_2$  increases, the nucleus becomes further elongated, and a slight neck appears. At the second saddle point, the neck becomes more pronounced, and the nucleus shows a tendency towards symmetric division. However, due to the inclusion of the reflection asymmetric degree of freedom, the ground state of  $^{240}\text{Pu}$  appears slightly pear-shaped in Fig. 2(b). As the deformation increases, similarly to Fig. 2(a), the nucleus begins to elongate along the  $z$  axis. But, by the second saddle point, the mass density distribution is reflection asymmetric, and the nucleus is more inclined towards mass-asymmetric fission. As seen in Fig. 1, mass asymmetry is mainly formed during the rapid descent following passing the outer barrier.

To further highlight the accuracy of our calculations, we have compared the results for the inner barrier height  $B_i$  and outer barrier height  $B_o$ , as well as the excitation energy  $E_{II}$  of the isomeric state relative to the ground state, with those obtained from other models. The results of the macroscopic-microscopic Woods-Saxon model [30], the Skyrme Hartree-Fock-Bogoliubov (SHFB) method [86], the multidimensionally constrained relativistic mean-field (MDC-RMF) model [71], and available experimental data [87,88] are presented in Table I. As shown in Table I, when reflection asymmetry is taken into account, the outer barrier height is reduced by 4.34 MeV compared to when reflection symmetry is assumed. In contrast, the inner barrier height and the excitation energy of the isomeric state remain nearly unchanged. This reduction in the outer barrier height emphasizes the

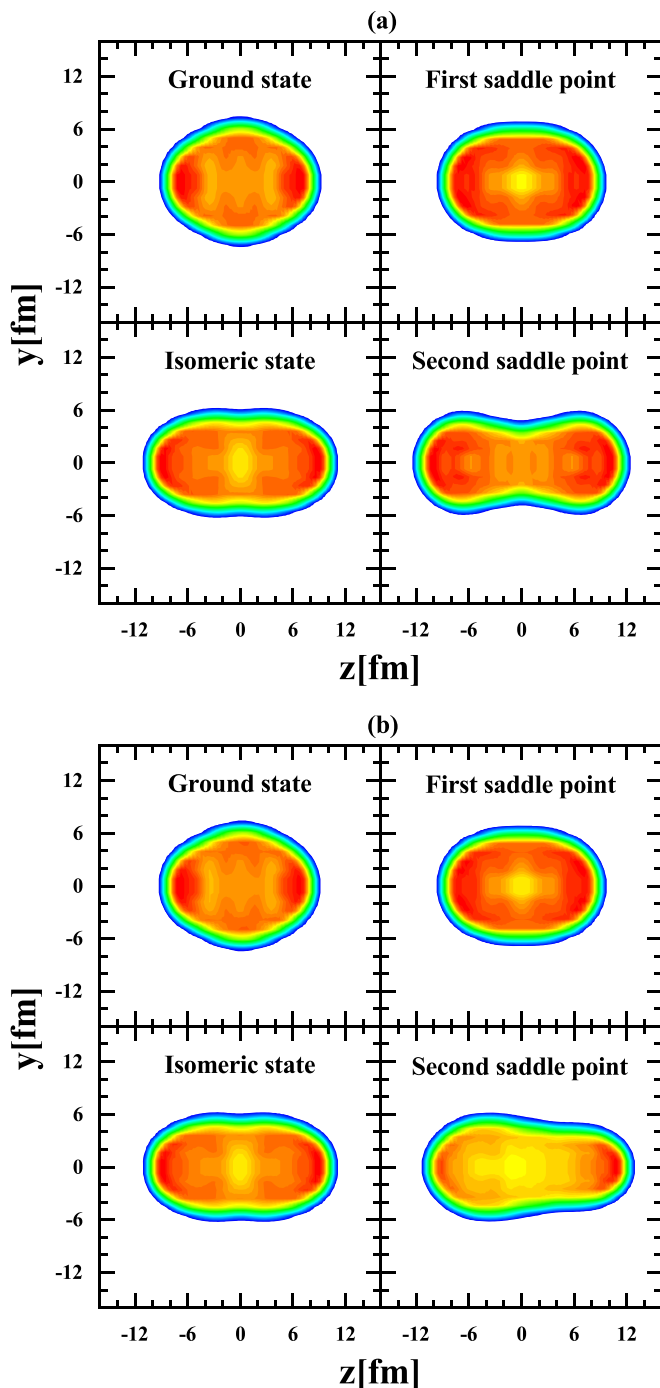


FIG. 2. Matter density distributions of  $^{240}\text{Pu}$  at the ground state, first saddle point, isomeric state, and second saddle point on the plane  $x = 0$ . Panel (a) is for reflection symmetry imposed, and panel (b) is for reflection asymmetry imposed with  $\beta_3 = -0.029$ . The parameter set used is NL3\*.

critical role that reflection asymmetric degree of freedom plays in accurately describing the static fission properties of actinide nuclei.

As we can see from our current calculations, they are in good agreement with experimental data and other theoretical models. For the inner barrier of  $^{240}\text{Pu}$ , the RSRMF, RASRMF,



TABLE I. The calculated inner barrier height ( $B_i$ ), outer barrier height ( $B_o$ ), and excitation energy ( $E_{II}$ ) of the isomeric state relative to the ground state in comparison with the experimental data and other theoretical calculations. The values in parentheses represent the results of the MDC-RMF calculation with triaxial deformation allowed. All quantities are given in MeV.

Model	$B_i$	$E_{II}$	$B_o$
RSRMF	6.50	1.72	9.63
RASRMF	6.34	1.62	5.29
MM [30]	6.61	1.94	5.71
SHFB [86]	9.32	2.59	6.46
MDC-RMF [71]	7.98	–	6.24
	(5.92)	–	(5.60)
Expt.	6.05 [88]	2.8 [87]	5.15 [88]

and MM calculations align more closely with experimental data. However, both the SHFB and MDC-RMF calculations significantly overestimate the barrier due to the absence of triaxial degree of freedom. It is worth noting that although triaxial deformation is also not included in our calculation, the result still aligns with experimental data. This is because there are many factors that influence the height of the barrier. In addition to deformations, the height of the fission barrier depends on the pairing interactions [38,86,89–91]. As shown in Table I, the difference between the calculated inner barrier height by the RASRMF and experimental data is 0.29 MeV, while the difference between the RSRMF calculation and experimental data is even larger (0.45 MeV). This deviation may be compensated by considering triaxial deformation.

For the outer barrier, since the effect of octupole deformation is considered in the calculation, the results from RASRMF, MDC-RMF, SHFB, and MM reproduce experimental data well. However, our result is closer to the data than those predicted by the other three theories. Accurately predicting the energy of the fission isomer is crucial for describing low-lying shape oscillations in actinide nuclei [92]. The SHFB calculation matches the experiment better compared to our calculation and the MM calculation. Further exploration is needed to understand why the theory underestimates the experimental value of the excitation energy of the isomeric state relative to the ground state.

In addition to deformation, the heights of the inner and outer barriers in nuclear fission are profoundly affected by pairing correlations. This phenomenon has been thoroughly examined in a series of earlier works [38,86,90,91]. As elucidated in Ref. [89], the fission barriers cannot be accurately described through the BCS approximation using a constant pairing gap. To confirm this assertion, the pairing gaps for protons and neutrons in  $^{240}\text{Pu}$ , as a function of the quadrupole deformation  $\beta_2$ , along the fission pathway derived from RASRMF calculations utilizing the NL3\* parameter set, are illustrated in Fig. 3. One can clearly see that the pairing gaps of neutrons and protons fluctuate significantly along the fission path. In particular, there is a relatively small pairing gap at the minima of the potential energy curve and a large pairing gap at the saddle point. This can be understood by

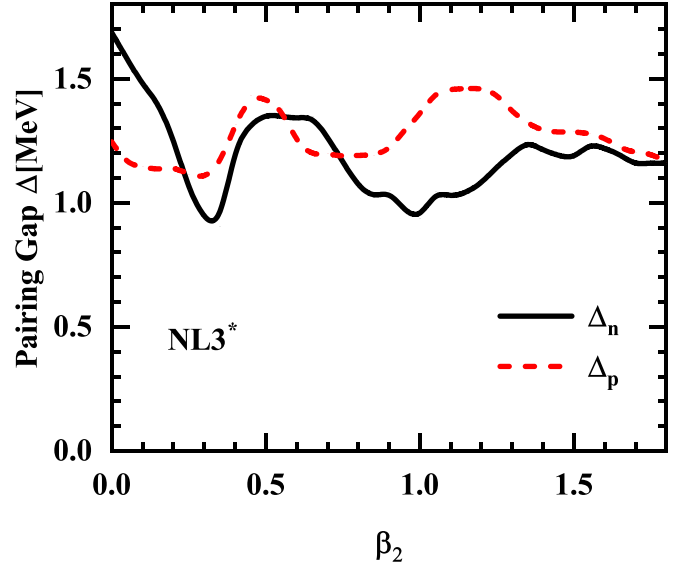


FIG. 3. The pairing gaps of neutrons and protons for  $^{240}\text{Pu}$  as a function of the quadrupole deformation  $\beta_2$ . These results are obtained in the RASRMF calculations with the parameter set NL3\*.

the fact [89] that the density of single-particle levels in the vicinity of the Fermi surface is changing considerably along the fission path. Since the pairing gap is closely linked to the level density [18], it cannot remain constant, and the calculations using the BCS approximation with a constant pairing gap will lead to nonphysical results for the fission barrier.

To affirm the superiority of our computation, which incorporates pairing correlations through the BCS approximation with a specified pairing strength, we have conducted a comparative analysis against RASRMF calculations employing the BCS approximation with a fixed pairing gap. The outcomes of this comparison are depicted in Fig. 4 for the nucleus  $^{240}\text{Pu}$ , utilizing the RASRMF framework with the NL1 [93] and NLSH [94] parameter sets. In the figure, the blue dashed curve represents the RASRMF+BCS computations utilizing a constant pairing gap, whereas the red dashed curve illustrates the results obtained with a fixed pairing strength. As Fig. 4 elucidates, the potential energy curve exhibiting a distinctive double-hump structure is accurately reproduced by the RASRMF model when applying both the NL1 and NLSH parameter sets in the calculation of  $^{240}\text{Pu}$ . This is achieved using the BCS approximation, whether with a fixed pairing gap or with a given pairing strength. However, it is noteworthy that the fission barrier height deduced from the BCS approximation with a constant pairing gap ( $\Delta$ ) is significantly elevated compared to that derived from a fixed pairing strength ( $G$ ), particularly in the RASRMF+BCS calculations utilizing the NL1 parameter set. This disparity underscores the critical importance of precise treatment of pairing correlations in achieving a reliable prediction of the fission barrier. Additionally, we have observed a systematic shift towards lower values in the deformation of all minima and barriers calculated with the NLSH parameter set relative to those computed with NL1, aligning with the findings reported in an earlier study

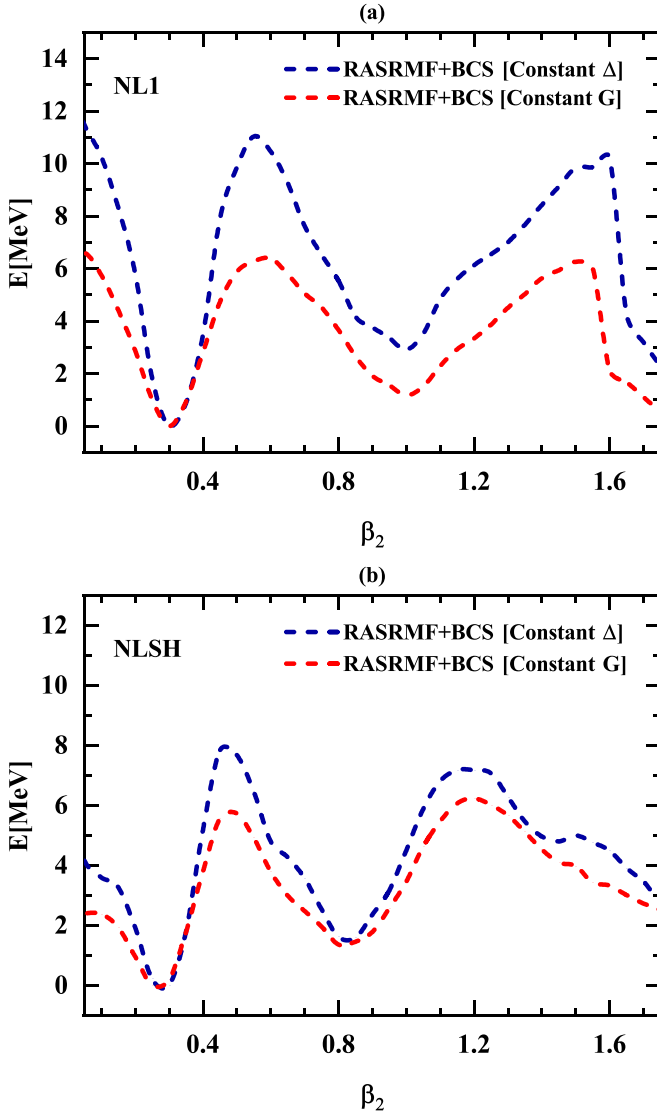


FIG. 4. The potential energy curves for  $^{240}\text{Pu}$  in the RASRMF calculations with the parameter sets NL1 [93] and NLSH [94]. The labels “constant  $\Delta$ ” and “constant  $G$ ” represent the BCS approximation with a constant pairing gap  $\Delta$  and a constant strength  $G$ , respectively. The results with NL1 and NLSH are respectively displayed in the upper and lower panels.

[46]. A plausible rationale for this discrepancy may lie in the increased effective mass associated with the NLSH parameter set, as previously suggested [45].

Numerical results on barriers and minima in Fig. 4 are summarized in Table II. For comparison, the result from the relativistic mean-field (RMF) calculations [46] and the experimental data are also listed there. It can be seen that the fission barriers obtained by the RASRMF calculations with a constant  $\Delta$  in the NL1 and NLSH parametrizations are comparable with those from the RMF calculations. However, when these theoretical results are contrasted with experimental data, they consistently overestimate the barrier heights. The introduction of triaxial deformation may be able to reduce the height of the inner barrier, but it is difficult to match the experimental value by considering triaxiality alone. Even including the reflection asymmetric degree of freedom in the RASRMF and RMF calculations, the outer barrier height is still higher than the experimental value. In contrast to the RASRMF calculations with a constant  $\Delta$ , the barriers obtained from the RASRMF calculations with a constant  $G$  demonstrate improved concordance with experimental results. This finding suggests that an appropriate treatment of pairing is essential for nuclear fission prediction based on CDFT. Compared with the BCS approximation with a constant pairing gap, the BCS approximation with a fixed pairing strength in the CDFT calculations is more accurate in describing the fission of the nucleus.

To understand the extent to which the fission barrier is affected by pairing interactions, we have calculated the potential energy curves of  $^{240}\text{Pu}$  with different pairing strengths using the RASRMF framework with the parameter set NL3\*. All energies were normalized relative to their ground-state value. As can be seen from Fig. 5, when the initial pairing interaction strengths  $G_n$  and  $G_p$  are changed from 96% to 104%, respectively, the potential energy curves become lower. Conversely, decreasing the pairing strength increases the energy of the isomeric state and the height of the inner and outer barriers, making it more difficult for the nucleus to undergo fission. Table III provides detailed values of the energies of the ground and isomeric states and the heights of the fission barriers for different pairing strengths, along with available experimental data for comparison. It was found that a slight increase in the pairing strength enhanced the stability of the

TABLE II. The ground state energy ( $E_{\text{g.s.}}$ ), inner barrier height ( $B_i$ ), outer barrier height ( $B_o$ ), and the excitation energy ( $E_{II}$ ) of the isomeric state relative to the ground state with different treatments of pairing (constant  $\Delta$ : constant pairing gap; constant  $G$ : constant pairing strength) obtained in the RASRMF calculations with the parameters NL1 [93] and NLSH [94] in comparison with the experimental data and other theoretical calculations. All quantities are given in MeV.

Model	Pairing correlation	Parameter set	$E_{\text{g.s.}}$	$B_i$	$E_{II}$	$B_o$
RASRMF	BCS(constant $\Delta$ )	NL1	-1813.55	11.03	2.91	10.23
		NLSH	-1818.99	7.82	1.59	7.17
	BCS(constant $G$ )	NL1	-1814.13	6.38	1.17	6.26
		NLSH	-1819.88	5.72	1.36	6.23
RMF [46]	BCS(constant $\Delta$ )	NL1	-1811.9	10.8	2.9	9.4
		NLSH	-1818.8	8.4	2.0	8.5
Expt.	-	-	-1813.45 [95]	6.05 [88]	2.8 [87]	5.15 [88]

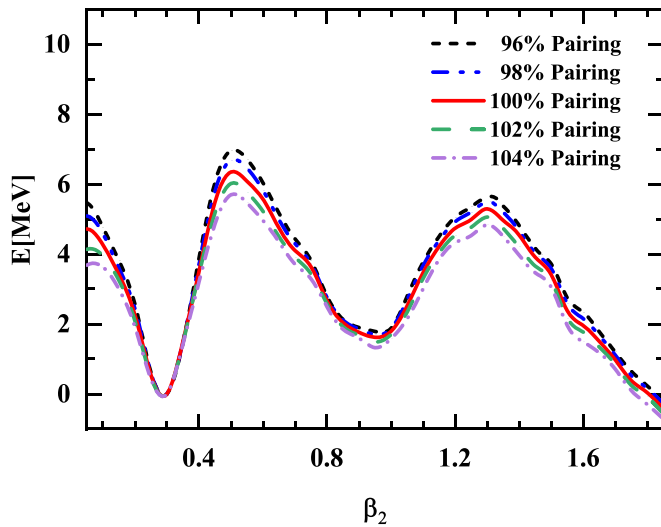


FIG. 5. The potential energy curves of  $^{240}\text{Pu}$  with different pairing strengths obtained in the RASRMF calculations. The parameter set used is NL3\*.

ground state, but reduced the fission barrier height, making the nucleus more conducive to fission due to pairing allowing for states to repopulate more effectively as the nucleus elongates [96]. Moreover, the energies of the ground state, isomeric state, and fission barrier obtained using the original pairing strengths match the experimental data better than those obtained from other pairing strengths. It should be mentioned that, in the calculation of the potential energy surface obtained by adding constraints, there are individual anomalies, possibly due to the collapse of the pairing correlations, which we have eliminated.

The potential energy curves of  $^{240}\text{Pu}$ , obtained through detailed studies, have emphasized the significant role of pairing interactions in understanding the fission properties of actinide nuclei. This has sparked interest in examining how sensitive the fission barriers are to variations in parameter sets, as explored in Refs. [57,97]. The potential energy curves of  $^{240}\text{Pu}$  calculated using the RASRMF method with three different parameter sets (NL3 [98], NL3\* [85], and PK1 [99]) are presented in Fig. 6, and the quantitative information from

TABLE III. The calculated energies for the ground state and those for the isomeric state and fission barrier relative to the ground-state value. The labels 96%, 98%, 100%, 102%, and 104% indicate the percentage relative to the original pairing strengths. All quantities are given in MeV. For comparison, experimental data are also listed in the last line.

	$E_{\text{g.s.}}$	$B_i$	$E_{II}$	$B_o$
96%	-1813.24	6.96	1.79	5.57
98%	-1813.57	6.68	1.70	5.49
100%	-1813.90	6.34	1.62	5.29
102%	-1814.29	6.02	1.49	5.05
104%	-1814.75	5.70	1.32	4.83
Expt.	-1813.45 [95]	6.05 [88]	2.8 [87]	5.15 [88]

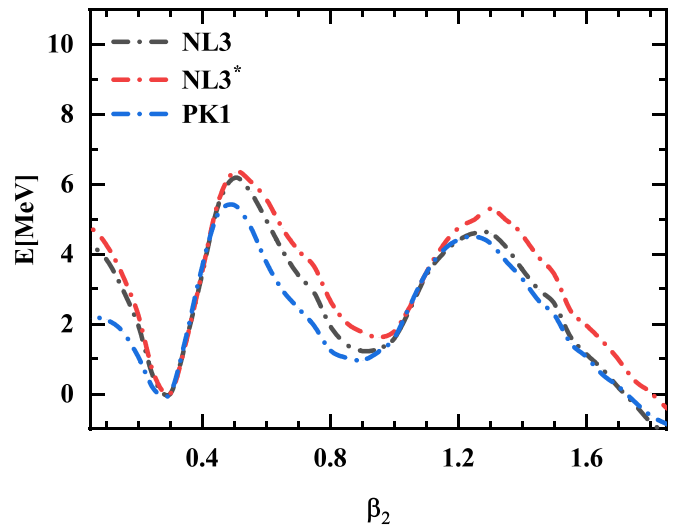


FIG. 6. The potential energy curves of  $^{240}\text{Pu}$  obtained in the RASRMF calculation with the three parameter sets NL3 [98], NL3\* [85], and PK1 [99].

these curves is summarized in Table IV. As can be seen from the figure, all the three calculations successfully reproduce the double-humped structure of  $^{240}\text{Pu}$ . However, there are some differences between the potential energy curves obtained from the calculations using different parameter sets. By comparing the results in Table IV, we observe that the inner barrier values calculated using NL3 and NL3\* are closer to experimental data. Nevertheless, for the outer barrier, only NL3\* provides a better prediction. Additionally, while the energy values of fission isomers calculated using all three parameter sets are lower than the experimental value, the result from NL3\* is more accurate than those of the other two parameter sets. The study shows that NL3\* provides a more accurate description of the static fission properties of  $^{240}\text{Pu}$  compared to the other two parameter sets.

#### IV. SUMMARY

In summary, the RASRMF theory was employed to investigate the static fission properties of actinide nuclei with  $^{240}\text{Pu}$  as an illustrated example. The conventional BCS approximation, which utilizes a specific pairing strength instead of a fixed pairing gap, is employed to manage pairing correlations.

TABLE IV. The available energies for the fission barrier and isomeric state in  $^{240}\text{Pu}$  in the RASRMF calculations with different parameter sets. The energies are expressed relative to their ground-state values. For reference, the experimental data are also included in the last line. All values are given in MeV.

Parameter set	$B_i$	$E_{II}$	$B_o$
NL3 [98]	6.17	1.22	4.59
NL3* [85]	6.34	1.62	5.29
PK1 [99]	5.40	0.95	4.49
Expt.	6.05 [88]	2.8 [87]	5.15 [88]

This method is considered more appropriate for depicting the fission process. The potential energy curves for  $^{240}\text{Pu}$  with reflection symmetry and reflection asymmetry were obtained. It was discovered that accounting for reflection asymmetry notably reduces the outer barrier of  $^{240}\text{Pu}$  compared to the symmetrical case. However, the fission pathway from the ground state to the isomeric state remains almost identical. This suggests that the degree of freedom associated with reflection asymmetry significantly impacts the outer barrier but has a minimal effect on the inner barrier and the second minimum.

The matter density distributions clearly illustrate the shape evolution of  $^{240}\text{Pu}$  along both the reflection-symmetric and reflection-asymmetric fission pathways. The inclusion of the reflection asymmetric degree of freedom favors mass-asymmetric fission for the nucleus. The mass asymmetry is mainly formed during the rapid descent after overcoming the outer barrier. It is evident that the reflection asymmetric degree of freedom not only reduces the height of the outer barrier but also significantly influences a fundamental characteristic of the mass distribution in fission products, whether it is symmetric or asymmetric.

The fission barrier heights obtained from the RASRMF calculations show agreement with empirical data and previous studies, with the exception of the SHFB approach, which significantly overestimates the inner barrier's height due to its neglect of triaxiality. It is worth noting that, despite the omission of triaxiality in the current calculations, the results still concur with empirical observations. This concurrence can be attributed to various factors affecting the barrier height, including deformations and pairing correlations. The model used for these computations does not adequately account for the impact of triaxiality at the saddle point configuration.

The role of pairing correlations in the fission process is investigated. It is observed that BCS calculations with a constant pairing strength ( $G$ ) result in significant fluctuations of the pairing gap ( $\Delta$ ) along the fission path. In contrast, the fission barriers derived from RASRMF and RMF calculations

with a fixed  $\Delta$  are notably higher than experimental data. Moreover, the barriers obtained from RASRMF calculations with a constant  $G$  show better agreement with experimental findings. These outcomes suggest that proper treatment of pairing correlations is crucial for accurate predictions of nuclear fission within the framework of CDFT. The current calculation employing a fixed  $G$  in the BCS approximation more accurately describes the fission of the nucleus compared to the BCS approximation with a constant  $\Delta$ , as referenced in other studies.

A slight increase in pairing strength enhanced ground state stability but lowered the fission barrier, favoring fission due to pairing allowing for states to repopulate more effectively as the nucleus elongates. Additionally, the dependence of fission barriers on parameter set was examined, and it was found that the RASRMF calculation with NL3\* provides a better description of the fission barriers for  $^{240}\text{Pu}$  than those with NL3 and PK1.

Overall, the predictive power of the RASRMF theory for static fission properties of actinide nucleus  $^{240}\text{Pu}$  is convincing when compared to experimental data and results from other models. Further systematic study of fission barriers of actinide nuclei using the RASRMF theory is necessary. Furthermore, future researches will consider the effect of triaxiality on fission barriers, as it has been shown to lower both the inner and outer barriers in previous studies. Additionally, forthcoming studies will embrace a more precise treatment of pairing through the application of the Bogoliubov transformation within the RASRMF framework.

## ACKNOWLEDGMENTS

This work was partly supported by the National Natural Science Foundation of China under Grants No. 11935001 and No. 11575002, the Key Research Foundation of Education Ministry of Anhui Province under Grant No. KJ2018A0028, and the Doctoral Scientific Research Startup Fund of Anhui University (Grant No. J01001319-J10113190082).

- 
- [1] M. Bender, R. Bernard, G. Bertsch, S. Chiba, J. Dobaczewski, N. Dubray, S. A. Giuliani, K. Hagino, D. Lacroix, Z. Li, P. Magierski, J. Maruhn, W. Nazarewicz, J. Pei, S. Péru, N. Pillet, J. Randrup, D. Regnier, P.-G. Reinhard, L. M. Robledo *et al.*, *J. Phys. G: Nucl. Part. Phys.* **47**, 113002 (2020).
  - [2] N. Schunck and D. Regnier, *Prog. Part. Nucl. Phys.* **125**, 103963 (2022).
  - [3] O. Hahn and F. Strassmann, *Naturwissenschaften* **27**, 11 (1939).
  - [4] L. Meitner and O. R. Frisch, *Nature (London)* **143**, 239 (1939).
  - [5] N. Bohr and J. A. Wheeler, *Phys. Rev.* **56**, 426 (1939).
  - [6] J. Zhao, B.-N. Lu, T. Nikšić, and D. Vretenar, *Phys. Rev. C* **92**, 064315 (2015).
  - [7] J. Zhao, B.-N. Lu, T. Nikšić, D. Vretenar, and S.-G. Zhou, *Phys. Rev. C* **93**, 044315 (2016).
  - [8] A. Bulgac, S. Jin, K. J. Roche, N. Schunck, and I. Stetcu, *Phys. Rev. C* **100**, 034615 (2019).
  - [9] Z. X. Ren, D. Vretenar, T. Nikšić, P. W. Zhao, J. Zhao, and J. Meng, *Phys. Rev. Lett.* **128**, 172501 (2022).
  - [10] Z. Li, S. Chen, Y. Chen, and Z. Li, *Phys. Rev. C* **106**, 024307 (2022).
  - [11] J. C. Pei, W. Nazarewicz, J. A. Sheikh, and A. K. Kerman, *Phys. Rev. Lett.* **102**, 192501 (2009).
  - [12] C.-J. Xia, B.-X. Sun, E.-G. Zhao, and S.-G. Zhou, *Sci. China Phys. Mech. Astron.* **54**, 109 (2011).
  - [13] A. Baran, M. Kowal, P. G. Reinhard, L. M. Robledo, A. Staszczak, and M. Warda, *Nucl. Phys. A* **944**, 442 (2015).
  - [14] A. V. Afanasjev, S. E. Agbemava, and A. Gyawali, *Phys. Lett. B* **782**, 533 (2018).
  - [15] M. Arnould and K. Takahashi, *Rep. Prog. Phys.* **62**, 395 (1999).
  - [16] A. Mamdouh, J. M. Pearson, M. Rayet, and F. Tondeur, *Nucl. Phys. A* **679**, 337 (2001).
  - [17] S. A. Giuliani, G. Martínez-Pinedo, and L. M. Robledo, *Phys. Rev. C* **97**, 034323 (2018).
  - [18] V. M. Strutinsky, *Nucl. Phys. A* **95**, 420 (1967).
  - [19] V. M. Strutinsky, *Nucl. Phys. A* **122**, 1 (1968).
  - [20] S. Bjørnholm and J. E. Lynn, *Rev. Mod. Phys.* **52**, 725 (1980).



- [21] V. V. Pashkevich, *Nucl. Phys. A* **133**, 400 (1969).
- [22] P. Möller and S. G. Nilsson, *Phys. Lett. B* **31**, 283 (1970).
- [23] T. Ledergerber and H.-C. Pauli, *Nucl. Phys. A* **207**, 1 (1973).
- [24] P. Möller, D. G. Madland, A. J. Sierk, and A. Iwamoto, *Nature (London)* **409**, 785 (2001).
- [25] P. Möller, A. J. Sierk, T. Ichikawa, A. Iwamoto, R. Bengtsson, H. Uhrenholt, and S. Aberg, *Phys. Rev. C* **79**, 064304 (2009).
- [26] T. Ichikawa, A. Iwamoto, P. Möller, and A. J. Sierk, *Phys. Rev. C* **86**, 024610 (2012).
- [27] M. Kowal, P. Jachimowicz, and A. Sobczewski, *Phys. Rev. C* **82**, 014303 (2010).
- [28] P. Jachimowicz, M. Kowal, and J. Skalski, *Phys. Rev. C* **85**, 034305 (2012).
- [29] P. Jachimowicz, M. Kowal, and J. Skalski, *Phys. Rev. C* **95**, 014303 (2017).
- [30] P. Jachimowicz, M. Kowal, and J. Skalski, *Phys. Rev. C* **101**, 014311 (2020).
- [31] A. Dobrowolski, K. Pomorski, and J. Bartel, *Phys. Rev. C* **75**, 024613 (2007).
- [32] K. Pomorski, B. Nerlo-Pomorska, J. Bartel, and C. Schmitt, *Phys. Rev. C* **97**, 034319 (2018).
- [33] Z. Wang, W. Zhu, C. Zhong, and T. Fan, *Nucl. Phys. A* **989**, 81 (2019).
- [34] H. Zanganeh, A. Kardan, and M. H. H. Yazdi, *Nucl. Phys. A* **997**, 121716 (2020).
- [35] A. Mamdouh, J. M. Pearson, M. Rayet, and F. Tondeur, *Nucl. Phys. A* **644**, 389 (1998).
- [36] A. K. Dutta, J. M. Pearson, and F. Tondeur, *Phys. Rev. C* **61**, 054303 (2000).
- [37] M. Kortelainen, J. McDonnell, W. Nazarewicz, P.-G. Reinhard, J. Sarich, N. Schunck, M. V. Stoitsov, and S. M. Wild, *Phys. Rev. C* **85**, 024304 (2012).
- [38] N. Schunck, D. Duke, H. Carr, and A. Knoll, *Phys. Rev. C* **90**, 054305 (2014).
- [39] N. Schunck, D. Duke, and H. Carr, *Phys. Rev. C* **91**, 034327 (2015).
- [40] C. Ling, C. Zhou, and Y. Shi, *Eur. Phys. J. A* **56**, 180 (2020).
- [41] M. Warda, J. L. Egido, L. M. Robledo, and K. Pomorski, *Phys. Rev. C* **66**, 014310 (2002).
- [42] J.-P. Delaroche, M. Girod, H. Goutte, and J. Libert, *Nucl. Phys. A* **771**, 103 (2006).
- [43] R. Rodríguez-Guzmán and L. M. Robledo, *Phys. Rev. C* **89**, 054310 (2014).
- [44] R. Rodríguez-Guzmán and L. M. Robledo, *Phys. Rev. C* **106**, 024335 (2022).
- [45] V. Blum, J. A. Maruhn, P.-G. Reinhard, and W. Greiner, *Phys. Lett. B* **323**, 262 (1994).
- [46] K. Rutz, J. A. Maruhn, P.-G. Reinhard, and W. Greiner, *Nucl. Phys. A* **590**, 680 (1995).
- [47] T. Bürvenich, M. Bender, J. A. Maruhn, and P.-G. Reinhard, *Phys. Rev. C* **69**, 014307 (2004).
- [48] S. E. Agbemava, A. V. Afanasjev, D. Ray, and P. Ring, *Phys. Rev. C* **95**, 054324 (2017).
- [49] S. E. Agbemava, A. V. Afanasjev, A. Taninah, and A. Gyawali, *Phys. Rev. C* **99**, 034316 (2019).
- [50] Z. Shi, A. V. Afanasjev, Z. P. Li, and J. Meng, *Phys. Rev. C* **99**, 064316 (2019).
- [51] X. Meng, B.-N. Lu, and S.-G. Zhou, *Sci. China Phys. Mech. Astron.* **63**, 212011 (2020).
- [52] D. Vretenar, A. V. Afanasjev, G. A. Lalazissis, and P. Ring, *Phys. Rep.* **409**, 101 (2005).
- [53] J. Meng, H. Toki, S. G. Zhou, S. Q. Zhang, W. H. Long, and L. S. Geng, *Prog. Part. Nucl. Phys.* **57**, 470 (2006).
- [54] T. Nikšić, D. Vretenar, and P. Ring, *Prog. Part. Nucl. Phys.* **66**, 519 (2011).
- [55] S. Shen, H. Liang, W. H. Long, J. Meng, and P. Ring, *Prog. Part. Nucl. Phys.* **109**, 103713 (2019).
- [56] L. Hong-Feng, G. Li-Sheng, and M. Jie, *Chin. Phys. Lett.* **23**, 2940 (2006).
- [57] H. Abusara, A. V. Afanasjev, and P. Ring, *Phys. Rev. C* **82**, 044303 (2010).
- [58] Z. P. Li, T. Nikšić, D. Vretenar, P. Ring, and J. Meng, *Phys. Rev. C* **81**, 064321 (2010).
- [59] B.-N. Lu, E.-G. Zhao, and S.-G. Zhou, *Phys. Rev. C* **85**, 011301(R) (2012).
- [60] V. Prassa, T. Nikšić, G. A. Lalazissis, and D. Vretenar, *Phys. Rev. C* **86**, 024317 (2012).
- [61] J. Zhao, B.-N. Lu, D. Vretenar, E.-G. Zhao, and S.-G. Zhou, *Phys. Rev. C* **91**, 014321 (2015).
- [62] H. Abusara, A. V. Afanasjev, and P. Ring, *Phys. Rev. C* **85**, 024314 (2012).
- [63] J.-F. Berger, Ph.D. thesis, Université Paris-Sud, 1985.
- [64] D. Regnier, N. Dubray, N. Schunck, and M. Verriere, *Phys. Rev. C* **93**, 054611 (2016).
- [65] D. Regnier, N. Dubray, and N. Schunck, *Phys. Rev. C* **99**, 024611 (2019).
- [66] Z. Li, S. Chen, M. Zhou, Y. Chen, and Z. Li, *arXiv:2309.03461*.
- [67] J. Randrup, S. E. Larsson, P. Möller, S. G. Nilsson, K. Pomorski, and A. Sobczewski, *Phys. Rev. C* **13**, 229 (1976).
- [68] M. Girod and B. Grammaticos, *Phys. Rev. C* **27**, 2317 (1983).
- [69] M. Bender, K. Rutz, P.-G. Reinhard, J. A. Maruhn, and W. Greiner, *Phys. Rev. C* **58**, 2126 (1998).
- [70] M. Bender, P.-H. Heenen, and P.-G. Reinhard, *Rev. Mod. Phys.* **75**, 121 (2003).
- [71] B.-N. Lu, J. Zhao, E.-G. Zhao, and S.-G. Zhou, *Phys. Rev. C* **89**, 014323 (2014).
- [72] S. A. Johansson, *Nucl. Phys.* **22**, 529 (1961).
- [73] N. Carjan, F. A. Ivanyuk, and Yu. Oganessian, *Nucl. Phys. A* **968**, 453 (2017).
- [74] G. Scamps and C. Simenel, *Nature (London)* **564**, 382 (2018).
- [75] G. Li-Sheng, M. Jie, and T. Hiroshi, *Chin. Phys. Lett.* **24**, 1865 (2007).
- [76] W. Zhang, Z. P. Li, S. Q. Zhang, and J. Meng, *Phys. Rev. C* **81**, 034302 (2010).
- [77] Y. T. Qiu, X. W. Wang, and J. Y. Guo, *Phys. Rev. C* **106**, 034301 (2022).
- [78] J. Y. Guo, P. Jiao, and X.-Z. Fang, *Phys. Rev. C* **82**, 047301 (2010).
- [79] H. Huang and J. Y. Guo, *Sci. Sin. Phys. Mech. Astron.* **43**, 69 (2013).
- [80] B. D. Serot and J. D. Walecka, *Adv. Nucl. Phys.* **16**, 1 (1986).
- [81] P. Ring, *Prog. Part. Nucl. Phys.* **37**, 193 (1996).
- [82] J. Meng, *Relativistic Density Functional for Nuclear Structure* (World Scientific, Singapore, 2016).
- [83] H. Tao, J. Zhao, Z. P. Li, T. Nikšić, and D. Vretenar, *Phys. Rev. C* **96**, 024319 (2017).
- [84] P. Ring and P. Schuck, *The Nuclear Many-Body Problem* (Springer-Verlag, New York, 1980).
- [85] G. A. Lalazissis, S. Karatzikos, R. Fossion, D. P. Arteaga, A. V. Afanasjev, and P. Ring, *Phys. Lett. B* **671**, 36 (2009).

- [86] Y.-J. Chen, Y. Su, G. Dong, L.-L. Liu, Z. Ge, and X. Wang, *Chin. Phys. C* **46**, 024103 (2022).
- [87] B. Singh, R. Zywna, and R. B. Firestone, *Nucl. Data Sheets* **97**, 241 (2002).
- [88] R. Capote, M. Herman, P. Oblozinsky, P. Young, S. Goriely, T. Belgia, A. Ignatyuk, A. Koning, S. Hilaire, V. Plujko, M. Avrigeanu, O. Bersillon, M. Chadwick, T. Fukahori, Z. Ge, Y. Han, S. Kailas, J. Kopecky, V. Maslov, G. Reffo *et al.*, *Nucl. Data Sheets* **110**, 3107 (2009).
- [89] S. Karatzikos, A. V. Afanasjev, G. A. Lalazissis, and P. Ring, *Phys. Lett. B* **689**, 72 (2010).
- [90] X. Guan, Y. Xin, Y. J. Chen, X. Z. Wu, and Z. X. Li, *Phys. Rev. C* **104**, 044329 (2021).
- [91] X. B. Wang, Y. J. Chen, G. X. Dong, Y. Su, Z. Y. Li, X. Z. Wu, and Z. X. Li, *Phys. Rev. C* **108**, 034306 (2023).
- [92] M. Kowal and J. Skalski, *Phys. Rev. C* **82**, 054303 (2010).
- [93] P.-G. Reinhard, M. Rufa, J. Maruhn, W. Greiner, and J. Friedrich, *Z. Phys. A* **323**, 13 (1986).
- [94] M. Sharma, M. Nagarajan, and P. Ring, *Phys. Lett. B* **312**, 377 (1993).
- [95] National Nuclear Data Center, <http://www.nndc.bnl.gov>.
- [96] G. Bertsch, *Phys. Lett. B* **95**, 157 (1980).
- [97] W. Ryssens, M. Bender, K. Bennaceur, P.-H. Heenen, and J. Meyer, *Phys. Rev. C* **99**, 044315 (2019).
- [98] G. A. Lalazissis, J. König, and P. Ring, *Phys. Rev. C* **55**, 540 (1997).
- [99] W. Long, J. Meng, N. Van Giai, and S.-G. Zhou, *Phys. Rev. C* **69**, 034319 (2004).